Biomaterials 300 (2023) 122201

Contents lists available at ScienceDirect

Biomaterials

journal homepage: www.elsevier.com/locate/biomaterials

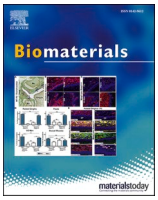

Multifunctional silk vinyl sulfone-based hydrogel scaffolds for dynamic material-cell interactions

Thomas Falcucci, Margaret Radke, Jugal Kishore Sahoo, Onur Hasturk, David L. Kaplan *

Tufts University, Department of Biomedical Engineering, Medford, MA, USA

ARTICLE INFO

Keywords:
Silk
Hydrogels
Click chemistry
Photochemistry
Fibrosis

ABSTRACT

Biochemical and mechanical interactions between cells and the surrounding extracellular matrix influence cell behavior and fate. Mimicking these features *in vitro* has prompted the design and development of biomaterials, with continuing efforts to improve tailorable systems that also incorporate dynamic chemical functionalities. The majority of these chemistries have been incorporated into synthetic biomaterials, here we focus on modifications of silk protein with dynamic features achieved via enzymatic, "click", and photo-chemistries. The one-pot synthesis of vinyl sulfone modified silk (SilkVS) can be tuned to manipulate the degree of functionalization. The resultant modified protein-based material undergoes three different gelation mechanisms, enzymatic, "click", and light-induced, to generate hydrogels for *in vitro* cell culture. Further, the versatility of this chemical functionality is exploited to mimic cell-ECM interactions via the incorporation of bioactive peptides and proteins or by altering the mechanical properties of the material to guide cell behavior. SilkVS is well-suited for use in *in vitro* culture, providing a natural protein with both tunable biochemistry and mechanics.

1. Introduction

The extracellular matrix (ECM) regulates and guides cell and tissue fate *in vivo*. [1] The ECM plays an essential role in tissue development and disease progression by providing physical and chemical cues that often change over time (e.g., development, disease, regeneration) to direct cell behavior [2–5]. This signaling is present during tissue repair, where injury-induced perturbations in homeostatic processes initiate a cascade of dynamic cell-ECM interactions to restore the tissue to the native state over time [6]. In fibrosis, this restorative process goes awry, where cell-ECM interactions perpetuate the disease toward a chronic state through dynamic feedback loops [4,7]. Namely, fibroblasts undergo a matrix-driven activation to myofibroblasts, a highly contractile and proliferative phenotype marked by α-smooth muscle actin (αSMA) expression, which has become a pathognomonic for fibrosis [8]. The path leading to either healthy or diseased tissue outcomes depends on the dynamic interplay involving matrix composition, biochemistry and mechanical cues, all of which influence cell behavior [9–13]. Thus, control of these dynamic tissue features is key when studying the underlying biology or developing *in vitro* tissue models of a disease.

Numerous biomaterial systems have been developed in an attempt to better capture the ECM microenvironment and to parse out the role of specific biochemical or physical cues in cell fate [9,14,15]. The biochemical composition [16], mechanical stiffness [17], and matrix architecture [10] of these materials were tuned to represent healthy and diseased tissue states in order to study biological principles that underly disease progression and tissue development *in vitro*. [15,18] While these materials highlighted the interplay between cells and their local extracellular environment, they often focus on one aspect of these tissue variables, and therefore do not account for the complexity and dynamic changes that occur during disease progression or tissue development [19]. Biomaterials that can more fully represent dynamic cell-ECM interactions should offer improved and more reliable *in vitro* systems for the study of tissue development and disease [20].

Polymeric materials capable of undergoing nanoscale changes and responses that emulate native tissue processes have been designed and engineered for use as biomaterials [9,14]. Early advancements focused on manipulating network formation and biochemical composition with stimuli such as temperature [21], pH [22], light [23,24], magnetic fields [25–27] or others [28]. However, modeling tissue *in vitro* requires increased spatiotemporal precision than these previous methods provide. Through interdisciplinary advancement, several chemistries have advanced the capabilities of *in vitro* models [29]. Generally, these chemistries are based on mechanisms such as click chemistry [12,

* Corresponding author.
E-mail address: david.kaplan@tufts.edu (D.L. Kaplan).

https://doi.org/10.1016/j.biomaterials.2023.122201
Received 20 January 2023; Received in revised form 5 June 2023; Accepted 7 June 2023
Available online 14 June 2023
0142-9612/© 2023 Elsevier Ltd. All rights reserved.

30–36], photochemistry [10,31,32,37–39], supramolecular principles [40–45], and biomolecular interactions [46–54].

As biomaterials diverge from static cultures toward complex, dynamic systems, diverse chemical functionality and mechanical tunability within a singular system are essential [9,40]. While the aforementioned chemistries have largely been limited to synthetic polymers, some natural materials have been chemically modified to contain advanced functionality, such as photocrosslinking [57], click chemistry [10], or supramolecular crosslinking [58]. However, these natural polymers usually are limited in mechanical integrity and versatility, often requiring the use of multicomponent systems.

Silk fibroin (termed silk hereafter) is a natural protein that forms mechanically robust, biocompatible, and versatile biomaterials [59]. Silk protein is an amphiphilic, high molecular weight polymer with highly repetitive glycine and alanine (GAGA) hydrophobic regions that are flanked by serine or tyrosines [60,61]. This structure controls the unique material properties by guiding self-assembly into β-sheet secondary structures which increase the mechanical strength of the material [62]. Past research has exploited this feature to generate hydrogels by inducing β-sheet crystallization to form robust, physically crosslinked networks or by employing enzymes to introduce free radicals on tyrosine side chains, which subsequently form dityrosine crosslinks [63–66]. While these features are useful, the structure of silk also limits the capacity to incorporate advanced chemical strategies to aid in the development of dynamic biomaterials for *in vitro* cell culture systems. There are a few examples of click [67–72] or photochemistry [73,74] translated to silk, however, these systems target reactive motifs in low abundance such as lysine side chains requiring the addition of a second polymer to increase available reactive sites or high polymer concentrations. Thus far, silk chemistry has been limited to the tyrosine motifs (~5.3 mol% of amino acids) or lysine and acidic side chains (~2 mol% combined) along the backbone [75–79]. While useful for representing some physiological ECM features, these chemistries alter the protein structure and the material properties, often rendering silk insoluble with low degrees of functionalization [78,80,81]. Alternatively, the serine groups, which account for ~12 mol% of the amino acids, have not been as actively pursued in terms of chemical modifications of silk [82,83].

Here, we aimed to introduce advanced chemical functionality to silk by exploiting serine moieties. The synthesis and characterization of silk modified with vinyl sulfone (SilkVS) was investigated. SilkVS can undergo both photocrosslinking and Michael-type "click" chemistry with thiol containing molecules at free vinyl sulfone groups while maintaining the previously established enzymatic reactivity at the tyrosine side chains. The various chemical functionalities provide several bioorthogonal methodologies for modifying the mechanical and biochemical features of the hydrogels formed from the modified silk. These properties are cell compatible and can be exploited to guide cell behavior by incorporating characteristic biochemical features of the ECM. Furthermore, the matrices formed can undergo secondary network formation which results in on-demand mechanical stiffening of the initial network. Examining cell behavior on these SilkVS matrices as a function of matrix stiffening, fibroblasts underwent phenotypic changes corresponding with native cell-ECM interactions.

2. Materials and methods

2.1. Synthesis vinyl sulfone-modified silk (SilkVS)

Aqueous silk solutions were prepared as previously described [84]. In short, *Bombyx mori* cocoons (Tajima Shoji Co., Ltd., Yokohama, Japan) were degummed to remove sericin protein by boiling 5 g of cut cocoons in 2 L of 0.02 M $NaCO_3$ (Sigma-Aldrich, St. Louis, MO, USA) for 60 min followed by thorough rinsing in deionized (DI) water. The degummed fibers were allowed to dry overnight before solubilizing in a 9.3 M LiBr solution at a concentration of 25%(w/v) for 4 h at 60 °C. The solution was then dialyzed against DI water using regenerated cellulose dialysis tubing (MWCO: 3500 Da, Spectra/Por®3 Standard RC Tubing, Spectrum Laboratories Inc., Rancho Dominguez, CA, USA). Over the course of 3 days, the dialysis water was changed 6 times. This solution was then centrifuged to remove any insoluble particulates and the concentration was calculated by measuring the mass of the silk that remained after drying a known volume of aqueous solution.

SilkVS was synthesized by first diluting the aqueous silk solution to 2%(w/v) in 0.1 M NaOH (Sigma-Aldrich, St. Louis, MO, USA). With constant vigorous stirring by a magnetic stir bar and a pH probe equipped, divinyl sulfone (DVS) (Sigma-Aldrich, St. Louis, MO, USA) was then added to the solution and a 5 min timer was started. The volume of DVS was calculated by determining the theoretical serine molar content on the silk which was then multiplied by R = 1.25, 2.5, or 5.0 to achieve the moles of DVS and then converted to a volume with the molar mass and density of DVS (Equation (S1)) [85]. During the reaction, the solution would start as a clear, slightly yellow solution and develop into a clear, slightly brown solution (depending on the degree of functionalization). After 5 min, the solution was neutralized to pH = 7.4 carefully with 10 and 1 M HCl dropwise. Caution was taken to add acid slowly and to ensure pH equilibrium before removing the sample from stirring as pH < 7 will induce β-sheet crystallization in silk. To remove any excess DVS, the SilkVS solution was then dialyzed against DI water using regenerated cellulose dialysis tubing (MWCO: 3500 Da, Spectra/Por®3 Standard RC Tubing, Spectrum Laboratories Inc., Rancho Dominguez, CA, USA) over 3 days with 6 water changes. This purification technique has been established to remove vinyl sulfone and purify chemically modified silk solutions [78,86–89]. The purified SilkVS solution was then concentrated to >10%(w/v) by hanging the tubing in a fume hood and allowing water to evaporate. Functionalization of SilkVS was confirmed by H^1 nuclear magnetic resonance (NMR) spectroscopy in deuterium oxide (D_2O) (Sigma-Aldrich, St. Louis, MO, USA) by observing a signal at δ = 6.18 corresponding to the vinyl hydrogen (Fig. S1) [88].

2.2. Characterization of SilkVS

Protein secondary structure and the degree of functionalization was analyzed by a JASCO FTIR 6200 spectrometer (JASCO, Tokyo, Japan) with a miracle attenuated total reflection germanium crystal. To prepare samples for FTIR, silk solutions were flash frozen at 1%(w/v) and then lyophilized for two days to produce a solid silk sponge. DVS solutions were prepared in a range of concentrations (0, 0.01,0.025, 0.05, 0.075, 0.1, 0.25, 0.5, 0.75, 1.0 mM) in DI water. A background of DI water was performed to isolate the signal from the DVS, respectively, in the solution. Spectra of the DVS solutions and solid sponge were obtained by averaging 32 scans with a resolution of 4 cm^{-1} within the wave number range of 600–4000 cm^{-1} (Fig. S3). The secondary structure was observed by comparing the amide I region (1600-1700 cm^{-1}) of unmodified silk (NSF) with SilkVS. The degree of functionalization was quantified using a custom MATLAB (MathWorks, Natick, MA, USA) script that normalized the sulfonyl peak signal, determined by taking the integral under the curve (1050-1200 cm^{-1}), to the amide I signal (1600-1700 cm^{-1}). A calibration curve was also created by associating FTIR absorbance at the sulfonyl peak with DVS concentration. This curve was then used to calculate the molar degree of functionalization of vinyl sulfone in a 3%(w/v) silk solution prepared from reconstituting the lyophilized sponges in DI water (Fig. S2).

To determine the molecular weight of the silk, gel electrophoresis was performed according to previous published work [90]. Here, 25 μL of 1%(w/v) unmodified silk (NSF) or SilkVS was mixed with 65 μL of LDS Sample Buffer (Invitrogen, NuPAGE, Waltham, MA, USA) and 10 μL of reducing agent. The solutions were vortexed and then heated at 70 °C in a dry heat bath for 10 min. After, 10 μL of each sample was loaded into a Bis-Tris-acetate gel along with two reference ladders Invitrogen, Novex Sharp-pre-stained Protein Standard, Waltham, MA, USA). Gels were then run at 200 V for 30 h in 1x MES-SDS running buffer (Thermo

Scientific, Waltham, MA, USA). The gel was then removed and fixed with a solution of 100 mL methanol, 20 mL acetic acid, and 80 mL DI water for 10 min. Colloidal blue stain (55 mL DI water, 20 mL methanol and 20 mL stain A (Invitrogen, Novex, Colloidal Blue Stain Kit, Waltham, MA, USA)) was then added for 15 min with gentle shaking. Then 5 mL of stain B (Invitrogen, Novex, Colloidal Blue Stain Kit, Waltham, MA, USA) was added and stained for 3 h with gentle shaking. The gel was then washed 3 times for 1 h and then overnight with DI water. The gel was then imaged. The molecular weight distributions were determined using ImageJ (1.48v, NIH, USA) software to calculate the pixel intensity as a function of pixel distance across the gel for each well. The standard ladder was used to create a standard curve of molecular weight vs pixel distance. The standard curve was then used to plot the molecular weight distribution for each sample as a function of pixel intensity. The distribution was then fit with a gaussian distribution, and the average molecular weight was determined (n = 3).

To quantify the concentration of primary amine and thiol motifs, two colorimetric assays were used. 2,4,6-Trinitrobenzene Sulfonic Acid (TNBSA) (Sigma-Aldrich, St. Louis, MO, USA) was used to quantify free primary amines. TNBSA was diluted 100x to 0.05% (w/v) in 0.2 M Na_2CO_3 (pH = 8.5). SilkVS and NSF was diluted to 0.5 mg/mL. The two solutions were then added at a 1:1 ratio and incubated at 37 °C for 2 h. 150 μL of the solution were then added to a clear 96 well plate and the absorbance at λ = 420 nm was measured on a plate reader. Solutions of known lysine concentrations were prepared and analyzed in the same way to create a standard curve correlating absorbance value and lysine content. To quantify thiols, the Ellman's reagent (ThermoFisher Scientific, Waltham, MA, USA) was performed according to manufacturers' protocol. Briefly, standards of L-cysteine were prepared in reaction buffer (0.1 M NaH_2PO_4, 1 mM EDTA, pH = 8.0) from a range of 1.5–0 mM. Meanwhile, 4 mg of Ellman's reagent was dissolved in 1 mL of reaction buffer. Then 250 μL of each standard was mixed with 2.5 mL of reaction buffer and 50 μL of the Ellman's reagent solution and incubated at room temperature for 15 min. The absorbance at λ = 420 nm was used to generate a standard curve of absorbance as a function of concentration. To determine the reaction kinetics of the thiol-ene chemistry, SilkVS solution was prepared at 7.5%(w/v) (pH = 7.8). 1 mM of L-cysteine (Sigma-Aldrich, St. Louis, MO, USA) was added to the SilkVS solution. Over 30 min, 250 μL of each sample were periodically removed and added to 50 μL of the Ellman's reagent solution and 2.5 mL of the reaction buffer. The absorbance at λ = 420 nm of each time point was then correlated with a thiol concentration and plotted as a function of time. The reaction kinetics were modeled based on a first-order decay to determine the reaction constants, k.

2.3. Hydrogel formation

Enzymatic crosslinking of silk and SilkVS hydrogels followed the protocol described elsewhere. Briefly, silk solutions were diluted in a 40 mM 2-[4-(2-hydroxyethyl) piperazin-1-yl] ethanesulfonic acid (HEPES) (Sigma-Aldrich, St. Louis, MO, USA), 5%(w/v) dextrose (Sigma-Aldrich, St. Louis, MO, USA) buffer with horseradish peroxidase (HRP) (Sigma-Aldrich, St. Louis, MO). The final concentrations of silk and HRP were 3%(w/v) and 10 U/mL, respectively. Then 10 μL of 1%(v/v) H_2O_2 (Sigma-Aldrich, St. Louis, MO) was added per 1 mL of the silk precursor solution to achieve a concentration of 0.01% (v/v) H_2O_2 and initiate gelation. The gel solution was then quickly pipetted into 96 well plates and incubated at 37 °C for 3 h to allow gelation to go to completion.

Michael-type "click" induced crosslinking was facilitated by initially creating a solution of silk at 7.5%(w/v) in 40 mM HEPES and 5%(w/v) dextrose (pH = 7.8). Meanwhile, a second solution of 100 mM dithiothreitrol (DTT) (Sigma-Aldrich, St. Louis, MO, USA) was prepared in DI H_2O. Then, the DTT solution was added to the silk solution at a 1:10 dilution and quickly mixed and aliquoted into molds. The solution was then incubated for 1 h at 37 °C to allow gelation to go to completion.

Photocrosslinked hydrogels were prepared by diluting silk solutions to 7.5%(w/v) in a solution of 0.02%(w/v) lithium phenyl-2,4,6-trimethylbenzoylphosphinate (LAP) (Sigma-Aldrich, St. Louis, MO, USA), 40 mM HEPES, and 5%(w/v) dextrose shielding the solution from light with aluminum foil. The solution was then pipetted into molds to and then exposed to 400 nm blue light for 2.5 min. The resultant gels were then rinsed 3 times for 30 min with Dulbecco's Phosphate Buffered Saline (DPBS) (ThermoFisher Scientific, Waltham, MA, USA).

To prepare the dual crosslinked hydrogels, enzymatic crosslinking was initially performed according to the aforementioned protocol with only SilkVS R = 2.5. Here, 40 μL of the precursor solution was pipetted into clear 96 well plates before incubating at 37 °C for 3 h. After incubation, 150 μL of a 0.025%(w/v) LAP in DI water solution was pipetted onto each gel and incubated at 37 °C for 1 h to facilitate diffusion of the photoinitiator into the hydrogel. Then, the solution was aspirated off the top of the hydrogel and the hydrogels were treated with 400 nm blue light for 2.5 min. The stiffened hydrogels were removed and treated with 1 mM RGD-SH for 1 h at 37 °C, rinsed 3 times for 30 min with DPBS, followed by 2 additional rinses with media facilitate cell adhesion and remove any remaining photoinitiator.

To prepare the Latent TGF-β1 (LTGF) decorated hydrogels, hydrogels were initially formed via enzymatic crosslinking according to the aforementioned protocol. The hydrogels were removed and treated with 1, 2, 5, 10, 20, 40 ng of LTGF dissolved in HD50 at pH 7.6 for 1 h at 37 °C, rinsed 3 times for 30 min with DPBS, followed by 2 additional rinses with serum containing media to facilitate cell adhesion and remove any remaining reagents.

2.4. Mechanical testing

Rheological properties were measured at 37 °C using an ARES HR10/20 rheometer (TA Instruments, New Castle, DE, USA). For the enzymatic and "click" crosslinking, the rheometer was equipped with a 40 mm stainless steel upper cone and the base was equipped with a temperature-controlled Peltier plate for the enzymatic and "click" crosslinking. A 420 μL aliquot of the hydrogel precursor solution was loaded onto the plate and the cone was lowered 47 μm, respectively. To initiate gelation, 4.2 μL of 1% H_2O_2 or 42 μL of 100 mM DTT, respectively, was added to the precursor solution during a10 s, 100 rad/s precycle. A dynamic time sweep was performed at 1 Hz with a 1% applied strain for 4000 s to determine gelation kinetics and storage moduli followed by dynamic frequency sweeps (0.1–100 rad/s at 1% strain) and strain sweeps (0.1% to failure at 1 Hz) to analyze the elastic properties of the hydrogels. For the photocrosslinking, the rheometer was equipped with a 20 mm stainless steel plate and the base was equipped with the UV plate and connected OmniCure UV lamp calibrate to 37.5 mW/cm^2. A 420 μL aliquot of the hydrogel precursor solution was loaded onto the plate and the cone or plate was lowered 1000 μm. To initiate the light source was turned on for 2.5 min. During light exposure, a dynamic time sweep was performed at 1 Hz with a 1% applied strain for 600s to determine gelation kinetics and storage moduli followed by dynamic frequency sweeps (0.1–100 rad/s at 1% strain) and strain sweeps (0.1% to failure at 1 Hz) to analyze the elastic properties of the hydrogels. Rheological properties were measured in the linear elastic region, where the storage modulus follow Newtonian behavior and was independent of applied strain.

Unconfined compression on all samples was performed on a TA Instruments RSA3 Dynamic Mechanical Analyzer (TA Instruments, New Castle, DE, USA) between 10 mm stainless steel parallel plates. Hydrogels were placed under a preload of ~0.5 g to ensure full surface contact. One load-unload cycles to 30% strain at a rate of 1% s^{-1} were performed to eliminate artifacts. Stress response and elastic recovery were monitored during a second load-unload cycle at the same strain rate. All moduli were calculated by taking the tangent modulus of the loading phase from 0 to 10% strain. Hydrogel precursor were cast into 12 mm diameter molds before adding H_2O_2 and allowing gelation to occur for 3 h at 37 °C. For the photo-stiffened hydrogels, the hydrogels were treated

with 0.025% (w/v) LAP in DI water for 1 h and then exposed to 400 nm blue light for 2.5 min. After, all gels were removed and shaped to 8 mm diameter samples (~2 mm height) using a biopsy punch (n = 5).

2.5. Cell culture

Human Normal Lung fibroblasts (ATCC, Manassas, VA, USA) were cultured in high-glucose Dulbecco's Modified Eagle's Medium (DMEM) (ThermoFisher Scientific, Waltham, MA, USA) supplemented with 1% antibiotic-antimycotic (ThermoFisher Scientific, Waltham, MA, USA), and, unless otherwise specified, 10% fetal bovine serum (FBS) (ThermoFisher Scientific, Waltham, MA, USA). Transforming growth factor-β1 (TGF-β1) was supplemented into the media, where specified, at 5 ng/mL. Culture media was replaced every three days before passaging. Hydrogels were prepared according to the methods described above; however, the precursor solutions were sterilized with a 0.22 μm sterile filter. Additionally, hydrogels treated with CGRGDS peptide (RGD-SH) (Genscript Biotech, Piscataway, NJ, USA) were incubated in a 1 mM solution in HEPES (pH = 7.8) for 1 h at 37 °C followed by 3 rinses with DPBS. All hydrogels from the stiffening experiment were treated with RGD-SH. Cells were dissociated before 5 passages and seeded onto the hydrogels 5000 cells cm^{-1}. To measure the metabolic activity of the cells on days 1, 3, 5, and 7 the gels were washed with DPBS and the cells were then treated with culture media containing 10% (v/v) AlamarBlue Reagent (ThermoFisher Scientific, Waltham, MA, USA) and incubated for 3 h at 37 °C. Following incubation, 150 μL aliquots of the supernatant media were transferred into opaque 96 well plates, and the fluorescence signal (ex: 560 nm, em: 590 nm) was measured using a microplate reader. Results were reported as the fold change in signal from day 1 (n = 5).

2.6. Fluorescent staining, microscopy, and analysis

To monitor the viability of the human lung fibroblasts cultured on the hydrogels, cells were stained with the Live/dead viability kit according to the manufacturers protocol and imaged with a BZ-X700 Fluorescence Microscope (Keyence Corp., Itasca, IL, USA). After incubating the cells with Ethidium homodimer-1 (EthD-1) and calcein-AM (ThermoFisher Scientific, Waltham, MA, USA) for 30 min, cells were rinsed with DPBS and imaged at day 7.

Studies investigating the cellular responses to treatment with RGD-SH were terminated at day 5. Studies investigating the cellular responses to treatment with mechanical stimuli and LTGF were terminated at day 6. At termination, cultures were fixed with 4% paraformaldehyde (ThermoFisher Scientific, Waltham, MA, USA) for 15 min at room temperature. To stain the actin cytoskeleton and nuclei, samples were permeabilized in PBS solution containing Triton X-100 (ThermoFisher Scientific, Waltham, MA, USA) (1% w/v) for 15 min; blocked in 1% bovine serum albumin (BSA) (ThermoFisher Scientific, Waltham, MA, USA) overnight; and stained simultaneously with phalloidin and 2'-(4-Ethoxyphenyl)-5-(4-methyl-1-piperazinyl)-2,5′-bi-1H-benzimidazole trihydrochloride (Hoechst 33342) (ThermoFisher Scientific, Waltham, MA, USA). For immunostaining, samples were permeabilized and blocked as mentioned then incubated with mouse monoclonal anti-αSMA (1:1000; Abcam ab7817, Waltham, MA, USA) for 3 h followed by donkey anti-mouse AlexaFluor 657 (1:2000; ThermoScientific Waltham, MA, USA) for 3 h with 3x PBS washes in between. Images were captured using a Leica SPX8 laser scanning confocal microscope with excitation wavelengths 405, 488, and 638 nm. Single cell protein analysis were performed using CellProfiler. Myofibroblasts were denoted as nucleated, F-actin$^+$, αSMA$^+$ cells. αSMA signal quantified as total fluorescence under each mask and thresholded according to the NSF, TGF-β1$^-$ controls. A similar method was used to quantify αSMA$^+$ fibroblasts [10]. For cell density calculations, Hoechst-stained cell nuclei were thresholded and counted.

2.7. Reverse transcription quantitative polymerase chain reaction (RT-qPCR)

For all experiments, cells were seeded on to 35 mm diameter hydrogels at 5000 cells/cm^2. Cells were lysed and RNA isolated using TRIzol (ThermoFisher Scientific, Waltham, MA, USA) reagent according to the manufacturers protocol. Complementary DNA (cDNA) was generated from deoxyribonuclease (DNase)-free RNA and amplified. Gene expression was normalized to the housekeeping gene hypoxanthine-guanine phosphoribosyltransferase (HPRT1). Experiments were run with three technical replicates. For a complete list of primers, see Fig. S11 (Azenta Life Sciences, Cambridge, MA, USA).

2.8. Statistical analysis

All data were expressed as means ± standard deviations. Sample size was indicated in the respective subsections. One- or two-way ANOVA (analysis of variance) with Tukey's post hos multiple comparison tests were performed using GraphPad Prism (GraphPad San Diego, CA, USA) unless specified otherwise. (*$p \leq 0.05$, **$p \leq 0.01$, ***$p \leq 0.001$).

3. Results

3.1. Silk vinyl sulfone (SilkVS) synthesis

SilkVS was synthesized according to the schematic in Fig. 1A. The serine and lysine groups were targeted by a one-pot synthesis under alkaline aqueous conditions. Divinyl sulfone (DVS) was added at 1.25, 2.5 and 5.0 M excess of the serines [85] (R = 1.25, 2.5 and 5.0, respectively) to control the degree of functionalization. H^1-NMR confirmed the addition of the vinyl group on the protein backbone with the δ = 6.28 ppm[88] (Fig. S1). Further, the reaction between serine motifs and the divinyl sulfone molecules is corroborated by the peak at δ = 3.5 ppm which corresponds to the ether formed during the reaction of the primary alcohol on serine and the vinyl sulfone group of DVS (Fig. 1A, S1). This was further corroborated with Fourier-transform infrared (FTIR) spectroscopy analysis, which showed distinct absorbance peak at 1131 cm^{-1} corresponding to the vinyl sulfone sulfoxide (S═O) bonds [91] (Fig. 1Bi). The FTIR spectra also shows absorbance peaks at 1600-1700 cm^{-1} which indicates the presence of the silk protein [92]. This region, known as the amide 1 region, appears on the spectra due to the secondary structure of the protein (i.e. random coils, α-helices, β-sheets, etc.). This region of the FTIR spectra confirms that the reaction conditions did not alter the secondary structure of silk (Fig. 1Bii, S3). In addition, FTIR spectra showed an increase in the abundance of the vinyl sulfone groups relative to the amide I signal (1600-1700 cm^{-1}) with increasing R-value (Fig. 1B, S2, S3). Further, analysis with a 2,4,6-Trinitrobenzene Sulfonic Acid (TNBSA) assay confirmed that primary amines of lysine moieties were consumed during the reaction, and there was a decrease in primary amine content with increasing R-value (Fig. 1D). Molecular weight distributions of the native, unmodified silk were compared to the vinyl sulfone modified silk (Fig. 1C, S4) to understand the impact of reaction conditions on the molecular weight. There was a slight increase in overall mean molecular weight as a function of R due to the addition of the vinyl sulfone groups (Fig. 1Cii).

3.2. Gelation of SilkVS

SilkVS polymer underwent enzymatic crosslinking based on *in situ* rheological (Fig. 2A and B) and fluorescence (Fig. S5) analyses where gelation was induced by the addition of horseradish peroxidase (HRP) and hydrogen peroxide (H_2O_2). There was an impedance of dityrosine crosslink formation compared to the native silk control and the formation of dityrosine bonds occurred at a reduced rate with increasing R-value (Fig. S5). In addition to enzymatic crosslinking, the material was also amenable to "click" chemistry as the available vinyl sulfone groups

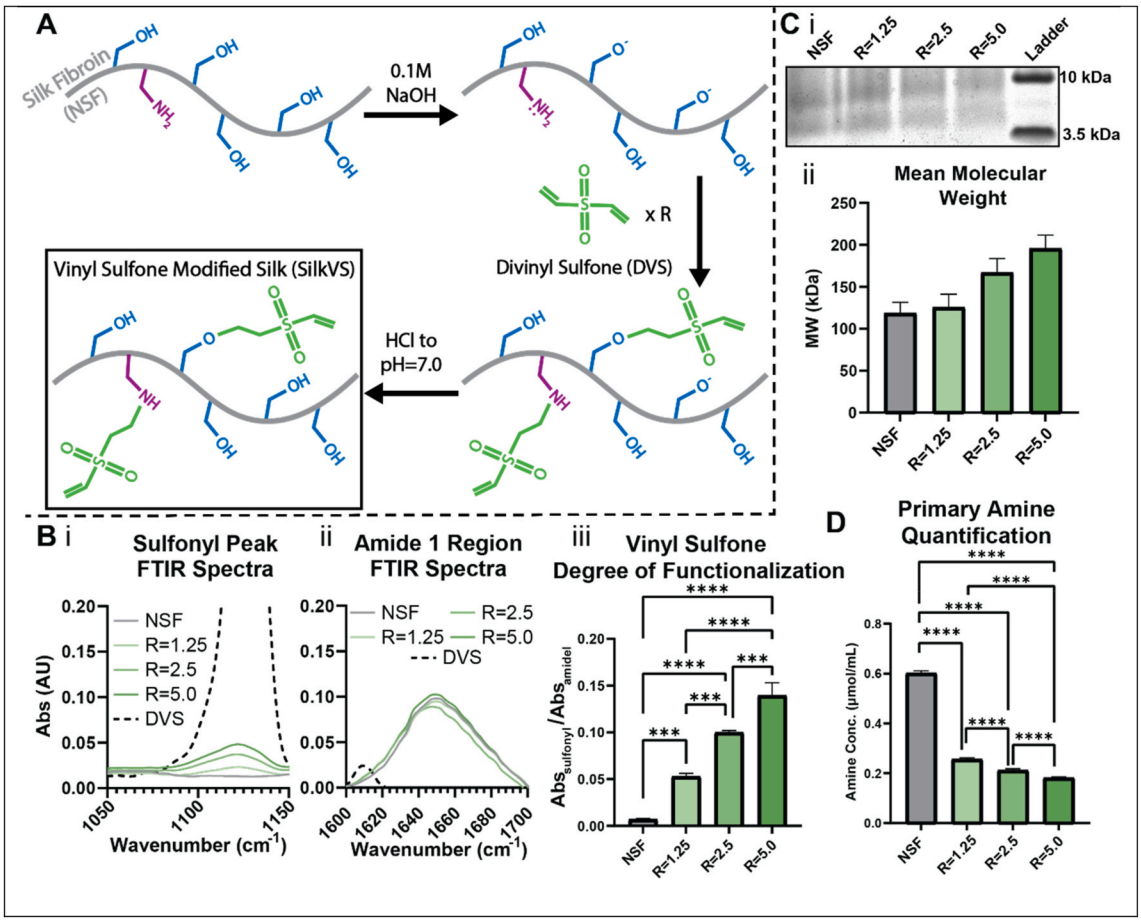

Fig. 1. ***Synthesis and Characterization of Vinyl Sulfone Modified Silk.*** (A) Native, unmodified silk (NSF) was reacted under basic conditions with various molar ratios (R) of divinyl sulfone (DVS) to generate SilkVS. (B) FTIR was used to quantify the degree of functionalization by normalizing the sulfonyl peak (i) to the amide I peak (ii) for each R-value (iii), n = 3. (C) SDS-PAGE analysis (i, representative image) of SilkVS and NSF were used to determine the mean molecular weights (ii), n = 3. (D) Primary amine content determined using TNBSA assay, n = 5. All data presented are means ± SDs.; *p ≤ 0.05, **p ≤ 0.01, ***p ≤ 0.005, ****p < 0.0001.

along the silk backbone are susceptible to Michael-type additions with free thiol groups (Fig. 2A). A thiol flanked molecule, 1,4-dithiothreitol (DTT), was used as a crosslinker to induce network formation. At pH 7.6, the thiols were activated, and gelation occurred in ~15 min after addition of the crosslinker (Fig. 2B). With increasing R-value, there was a reduction in gelation time. Furthermore, the kinetics of the thiol-ene Michael type addition, using L-cysteine as a model monothiol molecule, exhibited a similar increase in reaction rate with increasing R-value (Fig. S7).

Functionalization of silk with vinyl sulfone also enabled photocrosslinking by exploiting available vinyl groups to undergo free-radical crosslinking in the presence of a photoinitiator and blue light (400 nm) (Fig. 2A). Using lithium phenyl-2,4,6-trimethylbenzoylphosphinate (LAP) as the photoinitiator, there was an increase in shear modulus upon exposure to light, which correlated to network formation (Fig. 2B). The degree of functionalization guided the rate at which the modulus increased, with larger R-values forming networks at a faster rate.

3.3. Mechanical properties

The enzymatically crosslinked hydrogels had compressive moduli of 1.65 ± 0.06, 1.59 ± 0.08, 1.20 ± 0.17, and 1.08 ± 0.05 kPa for native silk and the R = 1.25, 2.5, and 5.0 hydrogels, respectively (Fig. 2C). The increased functionalization of SilkVS impeded dityrosine network formation and therefore reduced the compressive moduli. The opposite trend was found for both thiol-ene crosslinking and photocrosslinking. The hydrogels crosslinked with 0.2 mg/mL LAP and 1 min of blue light (λ = 400 nm) exposure had compressive moduli of 1.39 ± 0.068, 1.47 ± 0.11, and 1.78 ± 0.046 kPa for the R = 1.25, 2.5, and 5.0 hydrogels, respectively (Fig. 2C). SilkVS was crosslinked via thiol-ene click chemistry upon the addition of 10 mM DTT, the resultant compressive moduli were 0.82 ± 0.11, 1.57 ± 0.18, and 1.95 ± 0.13 kPa for the R = 1.25, 2.5, and 5.0 hydrogels, respectively (Fig. 2C). All gels demonstrated elastic behavior as indicated by the rheological frequency sweep and amplitude sweeps (Fig. S6).

3.4. Cytocompatibility

After validating the utility of SilkVS for generating hydrogels, cytocompatibility was assessed via Live/Dead staining and monitoring metabolic activity with AlamarBlue (Fig. 3B). All SilkVS material compositions supported increased metabolic activity over 7 days comparable to the unmodified native silk control. Live/dead image analysis showed minimal cell death in all conditions as represented by a low, red ethidium homodimer signal and high, green calcein signal (Fig. 3C).

3.5. Bioconjugation of SilkVS via thiol-ene "click" chemistry

The materials were engineered to display cell instructive ECM features (bioactive peptides and proteins) (Fig. 4A, C). Ellman's assay was used to characterize the "click" chemistry between the free vinyl groups of SilkVS and available thiol motifs by quantifying the concentration of thiols over time (Fig. 4Bi). When mixed with L-cysteine, the SilkVS rapidly consumed the thiol motifs, with the rate dependent on the

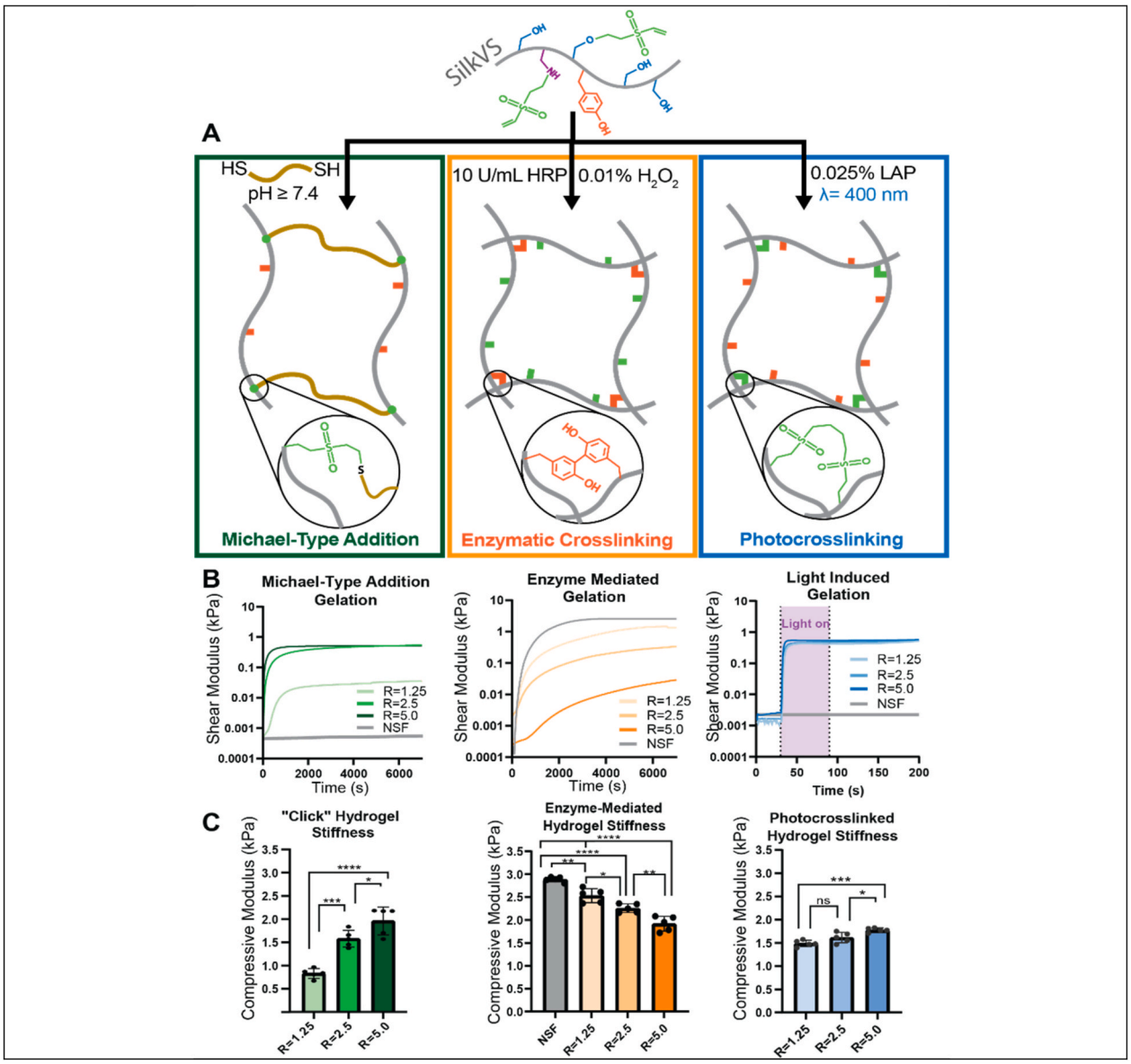

Fig. 2. ***Multiple Gelation Mechanisms of SilkVS.*** (A) SilkVS has the potential to crosslink via three distinct mechanisms: thiol-ene Michael-type addition (green) occurred in the presence of a dithiol molecule (DTT), enzymatically induced dityrosine formation (orange) in the presence of horseradish peroxidase (HRP) and H_2O_2, and photocrosslinking (blue) in the presence of a photoinitiator (LAP) and 400 nm blue light. (B) The gelation kinetics for each mechanism were tracked via *in situ* rheometry to monitor shear modulus (n = 3). (C) Compressive moduli of the hydrogels were measured (n = 5). All data presented are means ± SDs.; *p ≤ 0.05, **p ≤ 0.01, ***p ≤ 0.005, ****p < 0.0001. No significance unless otherwise indicated. (For interpretation of the references to color in this figure legend, the reader is referred to the Web version of this article.)

degree of functionalization of the SilkVS. The profile of thiols in solution was first order with increasing reaction constant, k, with increasing R value (Fig. S7). A cell binding peptide flanked by a cysteine group, CG**RGDS** (denoted RGD-SH), was then covalently bound to the network via the thiol-ene Michael type addition [10]. The same thiol quantification was run with RGD-SH to capture reaction kinetics of the peptide with SilkVS (R = 2.5) and the kinetic profile was comparable to the L-cysteine profile (Fig. S7). When translated to hydrogel culture, the absence of RGD-SH resulted in poor cell binding to the surface of native silk and SilkVS hydrogels. When RGD-SH was added, cell binding improved significantly for both systems. The former showed some cell adhesion at day 5 in culture, while the RGD–SH–SilkVS hydrogels had a comparatively higher cell density at day 5 (Fig. 4Bii, S8).

The use of RGD-SH peptide provided a proof-of concept for cell control related to cell binding, however more complex biochemical systems were pursued to further mimic features of the ECM.

Latent Transforming Growth Factor (LTGF)-β1, a protein complex that stores and releases TGF-β1 *in vivo* and is implicated in fibrotic disease progression, was employed [2]. The protein complex was bound to the SilkVS matrix via available thiol groups on the protein and the response of fibroblasts seeded on the hydrogel matrices was observed (Fig. 4C). Cellular responses to hydrogels treated with a range of LTGF concentrations (0.1 ng–40 ng) were observed. With increasing LTGF concentration, there was an increase in fibroblast myofibrotic activation, quantified by observing increased expression of α-smooth muscle actin (αSMA) (Fig. 4Di, ii). This myofibrotic activation is a biomarker for fibrosis. The extent of cell activation plateaued after exceeding 10 ng of LTGF (Fig. 4Dii).

3.6. Mechanical activation

Stiff hydrogels were formed by generating photoinduced secondary

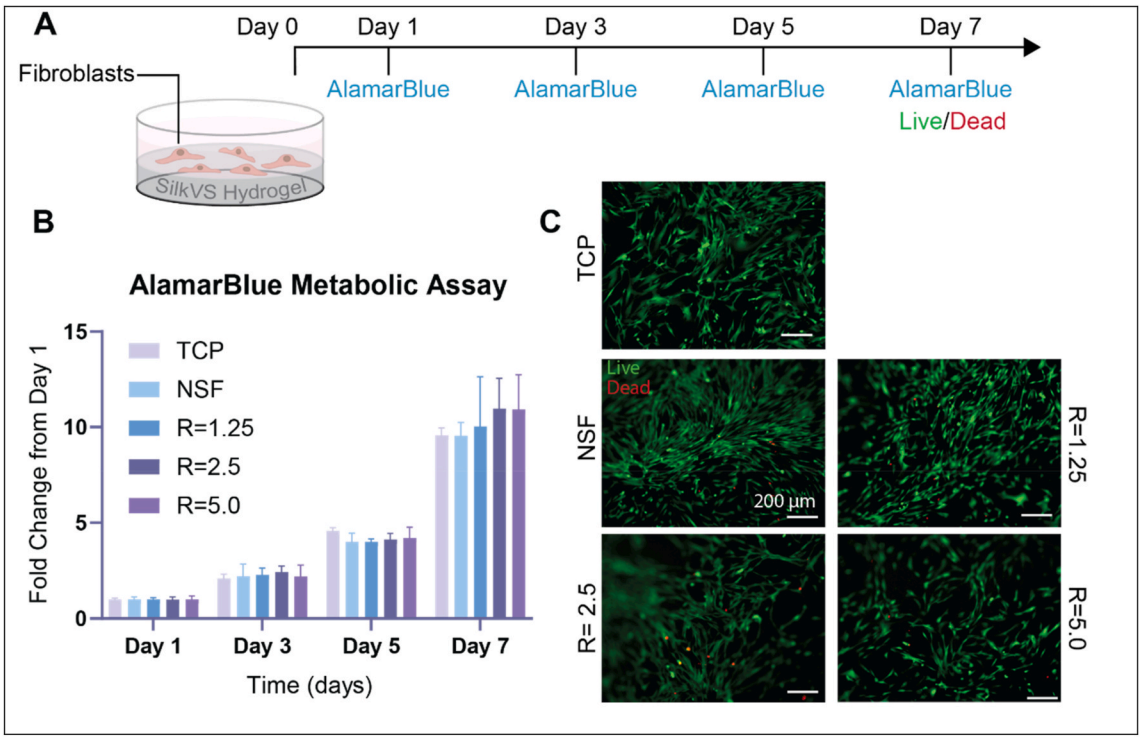

Fig. 3. ***SilkVS Hydrogel Cytocompatibility.*** (A) Cytocompatibility was assessed by seeding fibroblasts on enzymatically crosslinking SilkVS and native silk hydrogels and observing metabolic activity and viability. (B) Cell metabolism was assessed using AlamarBlue over 7 days (n = 5). (C) Cell viability was measured with fluorescence imaging where live cells were indicated by a green signal and cell death by red signal (C). Images are representative (n = 5) All data presented are means ± SDs.; *p ≤ 0.05, **p ≤ 0.01, ***p ≤ 0.005, ****p < 0.0001. No significance unless otherwise indicated. (For interpretation of the references to color in this figure legend, the reader is referred to the Web version of this article.)

networks. Hydrogels were initially prepared by exploiting the enzymatic crosslinking, followed by the formation of a secondary photocrosslinked network at the vinyl groups with 400 nm light and the photoinitiator LAP (Fig. 5A). This secondary network increased the compressive moduli of the hydrogels to 5.32 ± 0.69, 6.29 ± 0.728, and 8.04 ± 0.71 kPa for the R = 1.25, 2.5, and 5.0 hydrogels, respectively (Fig. 5B). Fibroblasts seeded on the soft untreated SilkVS matrix (R = 2.5) showed minimal myofibrotic activation as determined by quantifying the expression of αSMA. In contrast, fibroblasts seeded on the photostiffened hydrogels, representative of the mechanics of fibrotic tissue [93], supported increased cell spreading and more αSMA expression (Fig. 5Ci). Image analysis demonstrated that cells seeded on the stiffer matrices underwent increased myofibrotic activation (~70% of cells were αSMA^{+}) compared to the cells seeded on the softer matrix (~15% αSMA^{+}) (Fig. S9). This conclusion was corroborated by RT-qPCR analysis, which showed a significant increase in ACTA2 and COL1A genes associated with fibrosis, in cells exposed to the stiffer hydrogels (Fig. 5Cii).

To assess the interplay of mechanics and biochemical composition on disease progression, similar photostiffening treatments were performed with TGF-β1 supplemented into the growth media. The presence of TGF-β1 resulted in a significant increase in myofibrotic activation in all conditions (Fig. 5Ci). When combined with stiffened SilkVS matrices, there was an amplification of this activation; the fold change in gene expression was significantly upregulated for both ACTA2 and COL1A (Figure Cii).

4. Discussion

The pivotal role of the ECM in tissue development and disease progression continues to be investigated and new tools have been developed to better represent the physiological features of the processes involved [9,55,56]. Three-dimensional (3D) biomaterial systems have been integral to capturing cell-ECM interactions *in vitro*. Recent material systems aim to capture the dynamic properties of tissue development and disease pathology by employing unique chemical strategies that mimic these time-dependent changes during disease progression and provide control over the material properties during these dynamic conditions. Much of these chemistries harness "click", photo-, or supramolecular chemistries to enable bioorthogonal and dynamic control over the polymer network [19,40,54,56]. Here we explored the potential of silk protein-based biomaterial designs to represent biochemical and mechanical features of native ECM *in vitro*. We selected silk due to its unique chemistry, amphiphilicity, self-assembly features, and formation into materials with robust mechanical properties.

The chemical synthesis of SilkVS followed the schematic in Fig. 1A. Under basic conditions, the serine hydroxyl and lysine primary amine side chains were deprotonated forming reactive nucleophiles. In the presence of the electrophile divinyl sulfone (DVS), the nucleophilic alkoxides and primary amines reacted to form vinyl sulfone modified silk (SilkVS). This chemical mechanism has previously been used as a crosslinker in polysaccharide material networks such as hyaluronic acid (HA) or dextran [88,94]. However, by tuning the stoichiometry, the reaction can be saturated or terminated before crosslinking occurs, leaving unreacted vinyl sulfone groups for use in subsequent reactions. Moreover, it has been shown that the degree of functionalization can be controlled with three different parameters: time, DVS concentration, and pH [88]. An initial validation of the synthesis with several analytical techniques (H^{1}-NMR, FTIR, and TNBSA assay) confirmed that this chemistry can be translated to silk (Fig. 1B, D, S1, S2). Then, to avoid prolonged exposure and the risk of protein degradation in alkaline reaction conditions, DVS concentration was varied to tune the final degree of functionalization. Specifically, the value of R, which corresponds to the molar ratio of DVS to serine moieties in the silk backbone, was altered and characterization of the polymer product confirmed that the chemistry was tunable. This is useful as the degree of functionalization

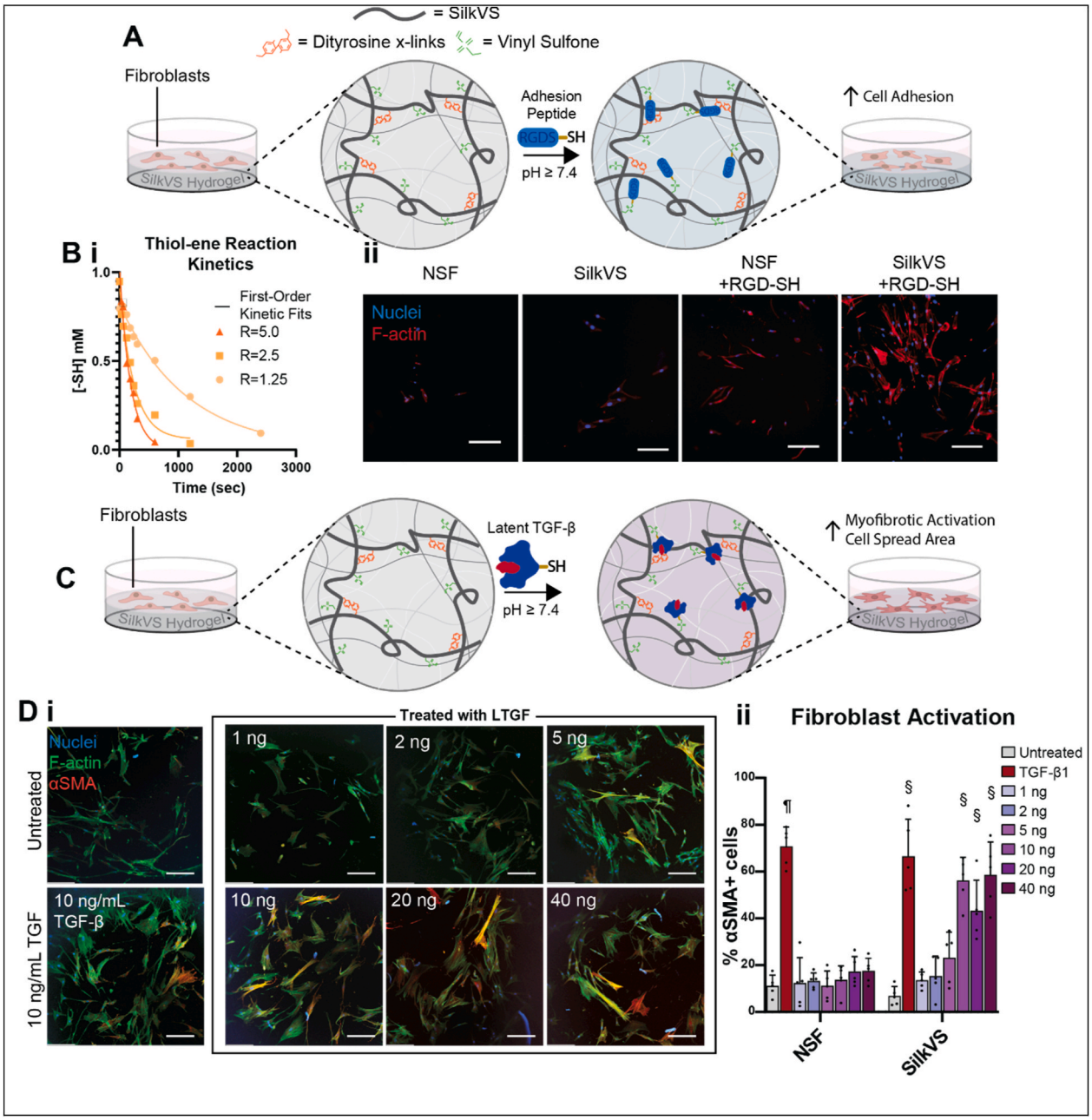

Fig. 4. ***Bioactive Molecules Decorate SilkVS Network to Guide Cell Behavior.*** (A) Thiol flanked cell adhesion peptide RGD-SH was displayed in the hydrogel network to guide cell adhesion on the SilkVS hydrogel. (Bi) Thiol-ene reaction kinetics between thiol containing molecules and SilkVS monitored using Elman's reagent. This chemistry was then used to "click" on RGD motifs to increase cell adhesion as indicated by images of cells on the hydrogel surfaces (ii) (n = 5). (C) A more complex and physiologically relevant biomolecule, latent TGF- β1 (LTGF), displayed on the surface at different concentrations. (D) Immunofluorescence imaging used to characterize fibroblast activation on the hydrogels in comparison to untreated and TGF-β1 treated controls (i) (n = 5). Images were analyzed to determine the number of activated cells as determined by αSMA^{+} expression (n = 5). Scale bars are 200 μm. All data presented are means ± SDs. Statistics are compared within the same condition group; no significance unless otherwise indicated; § indicates significant from all treatments other than those containing §, $p \leq 0.05$; ¶ indicates significant from all conditions, $p < 0.0001$.

can be altered to tune polymer structure which can then be exploited to manipulate the properties of the biomaterials formed (i.e., reactivity, mechanical, bioactivity).

While it was confirmed that vinyl sulfone was successfully conjugated onto the silk backbone, we next set out to confirm the functionality of the newly added motifs. It has been established that the tyrosine motifs that comprise the silk amino acid backbone form crosslinks in the presence of horseradish peroxidase (HRP) and hydrogen peroxide (H_2O_2) forming a hydrogel network [95]. With the conjugation of vinyl sulfone onto the silk backbone, this enzymatic functionality is expanded, incorporating a reactive motif that has been previously shown to undergo photo- and click chemistries (Fig. 2) [89]. Thiol-ene click crosslinking is useful for *in vitro* culture systems as it occurs rapidly within the range of physiological pH to ensure cell viability and homogeneity throughout the matrix [56]. Alternatively, the light-induced crosslinking allows for rapid crosslinking of the network within seconds of exposure to light. This is useful for *in vitro* culture systems, as well as for bioprinting ink because light allows for precise spatial control of crosslinking, however it is limited to small-scale material fabrication since absorption will increase with increasing penetration depth [96].

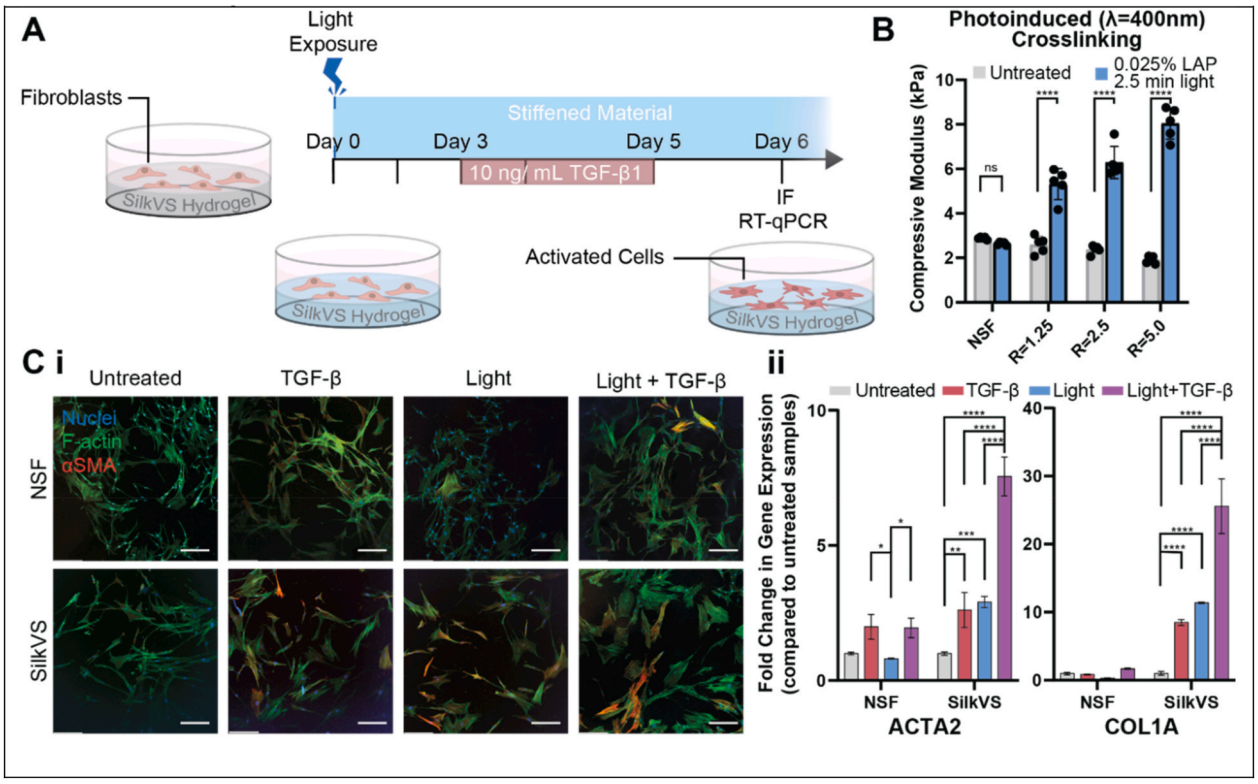

Fig. 5. ***Dual Crosslinked SilkVS Network Alters Mechanical Properties and Activates Fibroblasts.*** (A) SilkVS hydrogels undergo secondary network formation upon exposure to light (λ = 400 nm) and photoinitiator, LAP, resulting in stiffening of the matrix. (B) The extent of stiffening was characterized with compression testing for all SilkVS R-values (n = 5). (C) Fibroblasts seeded on R = 2.5 hydrogels and treated with light or TGF-β1 were imaged after 6 days to assess cellular activation by staining for αSMA and counter-staining the nuclei and F-actin (i). Images are representative (n = 5). RT-qPCR was performed on cells exposed to the various treatment conditions to characterize gene expression of ACTA2 and COL1A, two genes associated with fibrotic activation normalized to the housekeeping gene HPRT1 (ii) (n = 3). Scale bars are 200 μm. All data presented are means ± SDs.; *p ≤ 0.05, **p ≤ 0.01, ***p ≤ 0.005, ****p < 0.0001. No significance unless otherwise indicated.

When confirming the enzyme-mediated reactivity of SilkVS, it was shown that the tyrosine motifs are still available and functional. Interestingly, with increasing R-value, there was an observed inhibition of the gelation and reduction in the compressive moduli of the hydrogels (Fig. 2B, C, S5). This suggests that, while tyrosine moieties are not involved in the chemical synthesis, their functionality is altered in the resultant SilkVS molecules. This could be attributed to steric hinderances or quenching of the free radicals by the added vinyl sulfone motifs. Additionally, this slowed crosslinking allows for greater polymer chain rearrangement which would not only impact the final hydrogel mechanical properties, but also potentially alter the availability of the vinyl sulfone groups in the hydrogel network as they are not homogenously distributed across the silk backbone. Nonetheless, SilkVS formed a hydrogel in all conditions in the presence of HRP and H_2O_2, with minimal impact on hydrogel mechanics (Fig. 1C) confirming the modified protein maintains the previously established reactivity. The inhibition of enzymatic gelation contrasts with the click and photo-induced gelation of SilkVS both of which show accelerated gelation kinetics and increased mechanical properties with increasing R-value (Fig. 2). The resultant hydrogels had similar mechanics across SilkVS degrees of modification and showed elastic behavior (Fig. S6). Together, these data confirm that the conjugated vinyl sulfone groups are functional and demonstrate that the hydrogel properties can be tuned by controlling the degree of functionalization.

After validating the chemical synthesis and functionality of the materials, the feasibility of this material for *in vitro* cell culture was determined. Metabolic assessments and Live/Dead imaging of cells seeded on the hydrogel matrices confirmed that SilkVS was cytocompatible, regardless of the degree of functionalization, and provided a viable material for *in vitro* cell culture (Fig. 3). To ensure high vinyl sulfone functionality with practical enzymatic crosslinking times, R = 2.5 was selected for all cell culture experiments.

Next, to understand the potential of SilkVS for modeling biochemical features of the ECM *in vitro*, the functional polymer was exploited to bioorthogonally conjugate bioactive molecules onto the protein network. By exploiting the available vinyl sulfone motifs post-enzymatic crosslinking, the hydrogel network was decorated with RGD-SH peptides to control cell adhesion (Fig. 4A). RGD is an amino acid sequence found in several biomolecules like fibronectin, where it is was first discovered, and it is recognized by integrins on the surface of cells promoting cell adhesion [97]. When cultured without serum, cells minimally adhered to the surfaces as silk contains no native cell binding sites along its backbone [59]. Upon the addition of the RGD-SH peptide, there was increased cell adhesion to both the SilkVS and native silk matrices (Fig. 4Bi). While the latter is guided by peptide adsorption to the protein matrix, as shown by the reduced cell density, the former is a result of covalent binding to the SilkVS network at the vinyl sulfone motifs resulting in higher cell density (Fig. 4Bii, S8). This provided a demonstration of the ability to manipulate cell behavior by exploiting SilkVS chemistry to guide cell adhesion by displaying cell binding motifs, RGD-SH, along the polymer backbone.

To further elaborate on the potential of this system to mimic biochemical dynamics of disease, we exploited the thiol-ene chemistry to covalently bind latent transforming growth factor-β1 complex (LTGF) to the extracellular network (Fig. 4C). LTGF is a bioactive protein complex found in the ECM where a latency-associated peptide binds TGF-β1 sequestering the growth factor and releasing it upon injury [98–100]. While TGF-β1 is essential for homeostatic wound healing, it is

also a key biochemical factor in fibrotic diseases where it induces myofibrotic activation [101]. This growth factor is canonically supplemented in its active form into growth medium to study fibrotic activation *in vitro*; however, this supplementation is limited in representing the native cell-ECM interactions that guide growth factor release and activation [101,102]. Further, the presence of excess active TGF-β1 is implicated in diseases suggesting supplementation *in vitro* may cause undesirable study outcomes [103,104]. By incorporating LTGF into the matrix we aimed to better capture disease dynamics and cell-ECM interactions, highlighting the potential of this material network for use for *in vitro* disease models. When seeded onto the SilkVS matrix decorated with LTGF, fibroblasts underwent a myofibrotic activation, indicated by the increased production of αSMA (Fig. 4D). This response was not observed in the silk controls treated with the complex. This suggested that the growth factor binds to the network allowing cells to then interact with the ECM bound LTGF, resulting in the release of the TGF-β1 which then induces myofibrotic activation. This activation was dose-dependent, as αSMA expression increased with increasing LTGF. Interestingly, at LTGF concentrations above 10 ng per well, the cellular behavior appears to be independent of LTGF concentration (Figure Dii), suggesting that the cellular response was saturated. These results highlight the chemical functionality of the material which can be exploited to engineer *in vitro* systems that recapitulate native cell-ECM interactions.

We next set out to demonstrate the potential of the material for parsing out mechanical contributions of the ECM on physiological processes. Utilizing fibrosis as a model physiological process, we set out to capture the dynamic mechanical environment of the diseased tissue. A hallmark of fibrotic tissue is the formation of stiff scar tissue which stimulates stromal fibroblasts to undergo a phenotypic transition to the more contractile and active myofibroblasts marked by αSMA contractile fibers [14,105]. By exploiting the various crosslinking modalities available to SilkVS networks, we demonstrated that the material system captured the mechanical dynamics of diseases (Fig. 5B). Employing enzymatic crosslinking to generate a soft hydrogel reminiscent of healthy lung tissue mechanics and a secondary photocrosslinking to generate a stiff hydrogel that captures fibrotic tissue mechanics, changes in the matrix mechanics were utilized to replicate the mechanical activation of fibroblasts [10,14,17]. It is worth noting that both RGD-SH bioconjugation and photostiffening exploit the same reactive sites potentially impacting one another, so all photostiffening was performed prior to bioconjugation to preserve the material properties of the photosstiffened hydrogels. Nonetheless, fibroblasts underwent increased myofibrotic differentiation when cultured on the stiff light-treated substrates, whereas fibroblasts cultured on the soft untreated SilkVS and native silk hydrogels remained largely quiescent and inactivated (Fig. 5Ci, S10). This was corroborated by assessing the expression of fibrotic genes ACTA2 and COL1A, which showed that cells cultured on the dual crosslinked matrix underwent myofibrotic activation. Interestingly, when the biochemical contribution of the ECM was also considered by supplementing TGF-β1 into the mechanically dynamic system, we noted increased expression of both fibrotic genes (Fig. 5Cii). This suggested that the ECM biochemical composition works synergistically with the mechanical stimuli to exacerbate this diseased state. This conclusion highlights the importance of considering both the ECM biochemical composition and mechanical stimuli when designing an *in vitro* tissue model. Furthermore, the results suggest the potential of SilkVS for *in vitro* studies by providing a material system to control both the biochemical and mechanical extracellular environment.

This work outlines a "one-pot" chemical synthesis that exploits the relatively abundant serine motifs in silk to decorate the protein with vinyl sulfone groups enabling both photocrosslinking and thiol-ene "click" chemistry without inhibiting the enzymatic crosslinking potential of the protein. While there have been a few examples of click [67–72] or photochemistry [73,74] translated to silk, these systems target low abundant reactive motifs requiring the addition of a second polymer to increase available reactive sites or high polymer concentrations that are not feasible for *in vitro* cell encapsulation or bioprinting. This work provides the first example of a purely silk-based hydrogel system that employs click chemistry to form a hydrogel network. The resultant material exploits several crosslinking modalities to engineer the mechanical and biochemical composition of hydrogel scaffolds, with implication towards future three-dimensional studies and bioprinting fabrication techniques. When utilized as an *in vitro* culture system, the functionality lends itself to guiding cell behavior and parsing out the influence of different features of the extracellular environment, such as biochemistry and mechanics, on physiological processes with a single material system.

The versatility of silk-based materials and the results above contribute to the advancement of *in vitro* tissue modeling and tissue engineering, particularly toward developing tissue models of diseases where dynamic and complex cell-ECM interactions significantly impact outcomes, as in fibrosis. Analogous systems like poly(ethylene glycol) (PEG) or HA have established similar chemical modalities, however they require multistep syntheses involving harsh processing and result in material systems that are limited by their biocompatibility or mechanical integrity [43,106]. Herein, we strengthen silk as a viable biomaterial scaffold by developing a novel, facile chemical synthesis that imparts a range of functionality to the protein, suggesting a role in next generation biomaterials, engineered tissues and *in vitro* tissue models.

5. Conclusions

Silk was modified at serine and lysine side chains to incorporate vinyl sulfone functional groups. The vinyl sulfone modified silk (SilkVS) underwent hydrogel network formation via enzymatic, thiol-ene "click", and photochemistries. The multifunctional network was amendable to selective decoration with thiol containing molecules and dual network formation was observed upon exposure to blue light and a photoinitiator. During cell culture, the material supported cell growth and also allowed for control of cell behavior by altering the biochemical and mechanical environment. The results point to the novel utility of SilkVS for *in vitro* cell culture as the introduced functionality allows for bioorthogonal chemistry that can be used to mimic biochemical and mechanical environments of tissues during disease progression and development. Future use of this material can exploit this versatility to represent several tissues features in a single system allowing researchers to parse out the synergistic biological implications of the ECM with high fidelity. Additionally, SilkVS has the potential for use in bioprinting of soft tissue where the photocrosslinking capabilities can be exploited.

Credit author statement

Thomas Falcucci: Conceptualization, Methodology, Software, Formal Analysis, Investigation, Data Curation, Writing-Original Draft, Visualization, Project Administration **Margaret Radke:** Formal Analysis, Investigation, Data Curation, Writing-Review & Editing **Jugal Kishore Sahoo:** Conceptualization, Investigation, Data Curation, Writing-Review & Editing, Visualization **Onur Hasturk:** Conceptualization, Writing-Review & Editing **David L Kaplan:** Conceptualization, Resources, Writing-Review & Editing, Supervision, Project Administration, Funding Acquisition.

Declaration of competing interest

The authors declare that they have no known competing financial interests or personal relationships that could have appeared to influence the work reported in this paper.

Data availability

Data will be made available on request.

Acknowledgements

We thank the NIH (P41EB027062) for support of this work. The authors thank Rebecca Hershman, Sawnaz Shaidani, Olivia Foster, and Carmen Preda-Rucsanda for their technical help. For the use of their rheometer, the authors acknowledge the Harvard University Center for Nanoscale Systems (CNS); a member of the National Nanotechnology Coordinated Infrastructure Network (NNCI), which is supported by the National Science Foundation under NSF award no. ECCS-2025158.

Appendix A. Supplementary data

Supplementary data to this article can be found online at https://doi.org/10.1016/j.biomaterials.2023.122201.

References

[1] A.M. Rosales, K.S. Anseth, The design of reversible hydrogels to capture extracellular matrix dynamics, Nat. Rev. Mater. 1 (2016), 15012, https://doi.org/10.1038/natrevmats.2015.12.
[2] B. Hinz, The extracellular matrix and transforming growth factor-beta1: tale of a strained relationship, Matrix Biol. 47 (2015) 54–65, https://doi.org/10.1016/j.matbio.2015.05.006.
[3] N. Garamszegi, et al., Extracellular matrix-induced transforming growth factor-beta receptor signaling dynamics, Oncogene 29 (2010) 2368–2380, https://doi.org/10.1038/onc.2009.514.
[4] J.J. Tomasek, G. Gabbiani, B. Hinz, C. Chaponnier, R.A. Brown, Myofibroblasts and mechano-regulation of connective tissue remodelling, Nat. Rev. Mol. Cell Biol. 3 (2002) 349–363, https://doi.org/10.1038/nrm809.
[5] P. Pakshir, B. Hinz, The big five in fibrosis: macrophages, myofibroblasts, matrix, mechanics, and miscommunication, Matrix Biol. 68–69 (2018) 81–93, https://doi.org/10.1016/j.matbio.2018.01.019.
[6] N.C. Henderson, F. Rieder, T.A. Wynn, Fibrosis: from mechanisms to medicines, Nature 587 (2020) 555–566, https://doi.org/10.1038/s41586-020-2938-9.
[7] J.J. Saucerman, P.M. Tan, K.S. Buchholz, A.D. McCulloch, J.H. Omens, Mechanical regulation of gene expression in cardiac myocytes and fibroblasts, Nat. Rev. Cardiol. 16 (2019) 361–378, https://doi.org/10.1038/s41569-019-0155-8.
[8] P. Pakshir, et al., The myofibroblast at a glance, J. Cell Sci. 133 (2020) jcs227900, https://doi.org/10.1242/jcs.227900PMID-32651236.
[9] J. Lou, D.J. Mooney, Chemical strategies to engineer hydrogels for cell culture, Nat. Rev. Chem 6 (2022) 726–744, https://doi.org/10.1038/s41570-022-00420-7.
[10] D.L. Matera, et al., Microengineered 3D pulmonary interstitial mimetics highlight a critical role for matrix degradation in myofibroblast differentiation, Sci. Adv. 6 (2020), https://doi.org/10.1126/sciadv.abb5069.
[11] Jia, Y. et al. The Plasticity of Nanofibrous Matrix Regulates Fibroblast Activation in Fibrosis. Advanced Healthcare Materials **n/a**, 2001856, doi:https://doi.org/10.1002/adhm.202001856.
[12] N. Di Caprio, E. Bellas, Collagen stiffness and architecture regulate fibrotic gene expression in engineered adipose tissue, Adv Biosyst 4 (2020), e1900286, https://doi.org/10.1002/adbi.201900286.
[13] Y. Xu, et al., ECM-inspired micro/nanofibers for modulating cell function and tissue generation, Sci. Adv. 6 (2020), eabc2036, https://doi.org/10.1126/sciadv.abc2036.
[14] M.D. Davidson, J.A. Burdick, R.G. Wells, Engineered biomaterial platforms to study fibrosis, Adv Healthc Mater (2020), e1901682, https://doi.org/10.1002/adhm.201901682.
[15] R.C. Bretherton, C.A. DeForest, The art of engineering biomimetic cellular microenvironments, ACS Biomater. Sci. Eng. (2021), https://doi.org/10.1021/acsbiomaterials.0c01549.
[16] A.L. Wishart, et al., Decellularized extracellular matrix scaffolds identify full-length collagen VI as a driver of breast cancer cell invasion in obesity and metastasis, Sci. Adv. 6 (2020), eabc3175, https://doi.org/10.1126/sciadv.abc3175.
[17] C.J. Walker, et al., Author Correction: nuclear mechanosensing drives chromatin remodelling in persistently activated fibroblasts, Nat Biomed Eng (2021), https://doi.org/10.1038/s41551-021-00748-3.
[18] C.J. Walker, et al., Extracellular matrix stiffness controls cardiac valve myofibroblast activation through epigenetic remodeling, Bioeng. Trans. Med. 7 (2022), e10394, https://doi.org/10.1002/btm2.10394.
[19] B.A. Badeau, C.A. DeForest, Programming stimuli-responsive behavior into biomaterials, Annu. Rev. Biomed. Eng. 21 (2019) 241–265, https://doi.org/10.1146/annurev-bioeng-060418-052324.
[20] N.E. Félix Vélez, R.M. Gorashi, B.A. Aguado, Chemical and molecular tools to probe biological sex differences at multiple length scales, J. Mater. Chem. B 10 (2022) 7089–7098, https://doi.org/10.1039/D2TB00871H.
[21] L. Klouda, A.G. Mikos, Thermoresponsive hydrogels in biomedical applications, Eur. J. Pharm. Biopharm. 68 (2008) 34–45, https://doi.org/10.1016/j.ejpb.2007.02.025.
[22] S. Zhang, et al., A pH-responsive supramolecular polymer gel as an enteric elastomer for use in gastric devices, Nat. Mater. 14 (2015) 1065–1071, https://doi.org/10.1038/nmat4355.
[23] A.M. Rosales, K.M. Mabry, E.M. Nehls, K.S. Anseth, Photoresponsive elastic properties of azobenzene-containing poly(ethylene-glycol)-based hydrogels, Biomacromolecules 16 (2015) 798–806, https://doi.org/10.1021/bm501710e.
[24] L. Liu, et al., Cyclic stiffness modulation of cell-laden protein–polymer hydrogels in response to user-specified stimuli including light, Adv. Biosyst. 2 (2018), 1800240.
[25] D. Szabo, I.I. Czako-Nagy, M. Zrinyi, A. Vertes, Magnetic and mossbauer studies of magnetite-loaded polyvinyl alcohol hydrogels, J. Colloid Interface Sci. 221 (2000) 166–172, https://doi.org/10.1006/jcis.1999.6572.
[26] G. Filipcsei, J. Feher, M. Zrinyi, Electric field sensitive neutral polymer gels, J. Mol. Struct. 554 (2000) 109–117, https://doi.org/10.1016/S0022-2860(00)00564-0.
[27] H.M. Zlotnick, et al., Magneto-driven gradients of diamagnetic objects for engineering complex tissues, Adv. Mater. 32 (2020), e2005030, https://doi.org/10.1002/adma.202005030.
[28] A.M. Rosales, S.L. Vega, F.W. DelRio, J.A. Burdick, K.S. Anseth, Hydrogels with reversible mechanics to probe dynamic cell microenvironments, Angew. Chem. Int. Ed. 56 (2017) 12132–12136, https://doi.org/10.1002/anie.201705684.
[29] S. Correa, et al., Translational applications of hydrogels, Chem. Rev. 121 (2021) 11385–11457, https://doi.org/10.1021/acs.chemrev.0c01177.
[30] S.R. Caliari, et al., Gradually softening hydrogels for modeling hepatic stellate cell behavior during fibrosis regression, Integr. Biol. 8 (2016) 720–728, https://doi.org/10.1039/c6ib00027d.
[31] S.R. Caliari, et al., Stiffening hydrogels for investigating the dynamics of hepatic stellate cell mechanotransduction during myofibroblast activation, Sci. Rep. 6 (2016), 21387, https://doi.org/10.1038/srep21387.
[32] J.A. Shadish, C.A. DeForest, Site-selective protein modification: from functionalized proteins to functional biomaterials, Matter 2 (2020) 50–77, https://doi.org/10.1016/j.matt.2019.11.011.
[33] J.A. Shadish, A.C. Strange, C.A. DeForest, Genetically encoded photocleavable linkers for patterned protein release from biomaterials, J. Am. Chem. Soc. 141 (2019) 15619–15625, https://doi.org/10.1021/jacs.9b07239.
[34] H. Ma, A.S. Caldwell, M.A. Azagarsamy, A. Gonzalez Rodriguez, K.S. Anseth, Bioorthogonal click chemistries enable simultaneous spatial patterning of multiple proteins to probe synergistic protein effects on fibroblast function, Biomaterials 255 (2020), 120205, https://doi.org/10.1016/j.biomaterials.2020.120205.
[35] C.L. Petrou, et al., Clickable decellularized extracellular matrix as a new tool for building hybrid-hydrogels to model chronic fibrotic diseases in vitro, J. Mater. Chem. B 8 (2020) 6814–6826, https://doi.org/10.1039/D0TB00613K.
[36] W.M. Gramlich, I.L. Kim, J.A. Burdick, Synthesis and orthogonal photopatterning of hyaluronic acid hydrogels with thiol-norbornene chemistry, Biomaterials 34 (2013) 9803–9811, https://doi.org/10.1016/j.biomaterials.2013.08.089.
[37] A.R. Killaars, et al., Extended exposure to stiff microenvironments leads to persistent chromatin remodeling in human mesenchymal stem cells, Adv. Sci. 6 (2019), 1801483, https://doi.org/10.1002/advs.201801483.
[38] J.S. Silver, et al., Injury-mediated stiffening persistently activates muscle stem cells through YAP and TAZ mechanotransduction, Sci. Adv. 7 (2021) eabe4501, https://doi.org/10.1126/sciadv.abe4501.
[39] C.A. DeForest, D.A. Tirrell, A photoreversible protein-patterning approach for guiding stem cell fate in three-dimensional gels, Nat. Mater. 14 (2015) 523–531, https://doi.org/10.1038/nmat4219.
[40] C.J. Addonizio, B.D. Gates, M.J. Webber, Supramolecular “click chemistry” for targeting in the body, Bioconjugate Chem. 32 (2021) 1935–1946, https://doi.org/10.1021/acs.bioconjchem.1c00326.
[41] J. Hoque, N. Sangaj, S. Varghese, Stimuli-Responsive supramolecular hydrogels and their applications in regenerative medicine, Macromol. Biosci. 19 (2019), 1800259, https://doi.org/10.1002/mabi.201800259.
[42] G. Chen, M. Jiang, Cyclodextrin-based inclusion complexation bridging supramolecular chemistry and macromolecular self-assembly, Chem. Soc. Rev. 40 (2011) 2254–2266, https://doi.org/10.1039/C0CS00153H.
[43] C. Loebel, C.B. Rodell, M.H. Chen, J.A. Burdick, Shear-thinning and self-healing hydrogels as injectable therapeutics and for 3D-printing, Nat. Protoc. 12 (2017) 1521–1541, https://doi.org/10.1038/nprot.2017.053.
[44] M.J. Webber, E.A. Appel, E.W. Meijer, R. Langer, Supramolecular biomaterials, Nat. Mater. 15 (2016) 13–26, https://doi.org/10.1038/nmat4474.
[45] M. Rizwan, A.E.G. Baker, M.S. Shoichet, Designing hydrogels for 3D cell culture using dynamic covalent crosslinking, Advanced Healthcare Materials 10 (2021), 2100234, https://doi.org/10.1002/adhm.202100234.
[46] S. Ni, et al., Recent progress in aptamer discoveries and modifications for therapeutic applications, ACS Appl. Mater. Interfaces 13 (2021) 9500–9519, https://doi.org/10.1021/acsami.0c05750.
[47] D. Wang, Y. Hu, P. Liu, D. Luo, Bioresponsive DNA hydrogels: beyond the conventional stimuli responsiveness, Acc. Chem. Res. 50 (2017) 733–739, https://doi.org/10.1021/acs.accounts.6b00581.
[48] J.A. Hammer, J.L. West, Dynamic ligand presentation in biomaterials, Bioconjugate Chem. 29 (2018) 2140–2149, https://doi.org/10.1021/acs.bioconjchem.8b00288.
[49] Z. Sui, W.J. King, W.L. Murphy, Protein-based hydrogels with tunable dynamic responses, Adv. Funct. Mater. 18 (2008) 1824–1831, https://doi.org/10.1002/adfm.200701288.

[50] M.P. Lutolf, et al., Synthetic matrix metalloproteinase-sensitive hydrogels for the conduction of tissue regeneration: engineering cell-invasion characteristics, Proc. Natl. Acad. Sci. U.S.A. 100 (2003) 5413–5418.

[51] B.E. Turk, L.L. Huang, E.T. Piro, L.C. Cantley, Determination of protease cleavage site motifs using mixture-based oriented peptide libraries, Nat. Biotechnol. 19 (2001) 661–667, https://doi.org/10.1038/90273.

[52] A. Levin, et al., Biomimetic peptide self-assembly for functional materials, Nat. Rev. Chem 4 (2020) 615–634, https://doi.org/10.1038/s41570-020-0215-y.

[53] Z. Zhang, et al., Programmable integrin and N-cadherin adhesive interactions modulate mechanosensing of mesenchymal stem cells by cofilin phosphorylation, Nat. Commun. 13 (2022) 6854, https://doi.org/10.1038/s41467-022-34424-0.

[54] A.T. Speidel, C.L. Grigsby, M.M. Stevens, Ascendancy of semi-synthetic biomaterials from design towards democratization, Nat. Mater. 21 (2022) 989–992, https://doi.org/10.1038/s41563-022-01348-5.

[55] V.G. Muir, J.A. Burdick, Chemically modified biopolymers for the formation of biomedical hydrogels, Chem. Rev. 121 (2021) 10908–10949, https://doi.org/10.1021/acs.chemrev.0c00923.

[56] E. Hui, J.L. Sumey, S.R. Caliari, Click-functionalized hydrogel design for mechanobiology investigations, Molecular Systems Design & Engineering 6 (2021) 670–707, https://doi.org/10.1039/D1ME00049G.

[57] I. Batalov, K.R. Stevens, C.A. DeForest, Photopatterned biomolecule immobilization to guide three-dimensional cell fate in natural protein-based hydrogels, Proc. Natl. Acad. Sci. U. S. A. 118 (2021), https://doi.org/10.1073/pnas.2014194118.

[58] A.C. Daly, M.D. Davidson, J.A. Burdick, 3D bioprinting of high cell-density heterogeneous tissue models through spheroid fusion within self-healing hydrogels, Nat. Commun. 12 (2021) 753, https://doi.org/10.1038/s41467-021-21029-2.

[59] C. Li, et al., Design of biodegradable, implantable devices towards clinical translation, Nat. Rev. Mater. 5 (2020) 61–81, https://doi.org/10.1038/s41578-019-0150-z.

[60] W. Huang, S. Ling, C. Li, F.G. Omenetto, D.L. Kaplan, Silkworm silk-based materials and devices generated using bio-nanotechnology, Chem. Soc. Rev. 47 (2018) 6486–6504, https://doi.org/10.1039/C8CS00187A.

[61] C.Z. Zhou, et al., Silk fibroin: structural implications of a remarkable amino acid sequence, Proteins 44 (2001) 119–122, https://doi.org/10.1002/prot.1078.

[62] Y. Qi, et al., A review of structure construction of silk fibroin biomaterials from single structures to multi-level structures, Int. J. Mol. Sci. 18 (2017) 237.

[63] B.P. Partlow, et al., Highly tunable elastomeric silk biomaterials, Adv. Funct. Mater. 24 (2014) 4615–4624, https://doi.org/10.1002/adfm.201400526.

[64] B.P. Partlow, M.B. Applegate, F.G. Omenetto, D.L. Kaplan, Dityrosine cross-linking in designing biomaterials, ACS Biomater. Sci. Eng. 2 (2016) 2108–2121, https://doi.org/10.1021/acsbiomaterials.6b00454.

[65] H. Zheng, B. Zuo, Functional silk fibroin hydrogels: preparation, properties and applications, J. Mater. Chem. B 9 (2021) 1238–1258, https://doi.org/10.1039/D0TB02099K.

[66] J. Chakraborty, X. Mu, A. Pramanick, D.L. Kaplan, S. Ghosh, Recent advances in bioprinting using silk protein-based bioinks, Biomaterials 287 (2022), 121672, https://doi.org/10.1016/j.biomaterials.2022.121672.

[67] H. Zhao, et al., Decoration of silk fibroin by click chemistry for biomedical application, J. Struct. Biol. 186 (2014) 420–430, https://doi.org/10.1016/j.jsb.2014.02.009.

[68] D. Harvey, P. Bardelang, S.L. Goodacre, A. Cockayne, N.R. Thomas, Antibiotic spider silk: site-specific functionalization of recombinant spider silk using "click" chemistry, Adv. Mater. 29 (2017), 1604245, https://doi.org/10.1002/adma.201604245.

[69] X. Zhang, et al., Surface modification of Bombyx mori silk fibroin film via thiol-ene click chemistry, Processes 8 (2020) 498.

[70] X. Zhang, et al., Chemical modification of Bombyx mori silk fibers with vinyl groups for thiol-ene click chemistry, BMC Chemistry 13 (2019) 114, https://doi.org/10.1186/s13065-019-0630-7.

[71] J. Liang, X. Zhang, Z. Chen, S. Li, C. Yan, Thiol–ene click reaction initiated rapid gelation of PEGDA/silk fibroin hydrogels, Polymers 11 (2019) 2102.

[72] S. Ryu, et al., Dual mode gelation behavior of silk fibroin microgel embedded poly (ethylene glycol) hydrogels, J. Mater. Chem. B 4 (2016) 4574–4584, https://doi.org/10.1039/C6TB00896H.

[73] S.H. Kim, et al., 3D bioprinted silk fibroin hydrogels for tissue engineering, Nat. Protoc. 16 (2021) 5484–5532, https://doi.org/10.1038/s41596-021-00622-1.

[74] X. Mu, J.K. Sahoo, P. Cebe, D.L. Kaplan, Photo-crosslinked silk fibroin for 3D printing, Polymers 12 (2020) 2936.

[75] A.R. Murphy, D.L. Kaplan, Biomedical applications of chemically-modified silk fibroin, J. Mater. Chem. 19 (2009) 6443–6450, https://doi.org/10.1039/B905802H.

[76] K.G. Hausken, et al., Quantitative functionalization of the tyrosine residues in silk fibroin through an amino-tyrosine intermediate, Macromol. Chem. Phys. 223 (2022), 2200119, https://doi.org/10.1002/macp.202200119.

[77] J. Choi, M. McGill, N.R. Raia, O. Hasturk, D.L. Kaplan, Silk hydrogels crosslinked by the fenton reaction, Adv Healthc Mater 8 (2019), e1900644, https://doi.org/10.1002/adhm.201900644.

[78] O. Hasturk, K.E. Jordan, J. Choi, D.L. Kaplan, Enzymatically crosslinked silk and silk-gelatin hydrogels with tunable gelation kinetics, mechanical properties and bioactivity for cell culture and encapsulation, Biomaterials 232 (2020), 119720, https://doi.org/10.1016/j.biomaterials.2019.119720.

[79] O. Hasturk, J.K. Sahoo, D.L. Kaplan, Synthesis and characterization of silk ionomers for layer-by-layer electrostatic deposition on individual mammalian cells, Biomacromolecules 21 (2020) 2829–2843, https://doi.org/10.1021/acs.biomac.0c00523.

[80] A.R. Murphy, P. St John, D.L. Kaplan, Modification of silk fibroin using diazonium coupling chemistry and the effects on hMSC proliferation and differentiation, Biomaterials 29 (2008) 2829–2838, https://doi.org/10.1016/j.biomaterials.2008.03.039.

[81] M. McGill, J.M. Grant, D.L. Kaplan, Enzyme-mediated conjugation of peptides to silk fibroin for facile hydrogel functionalization, Ann. Biomed. Eng. (2020), https://doi.org/10.1007/s10439-020-02503-2.

[82] D.L. Heichel, K.A. Burke, Enhancing the carboxylation efficiency of silk fibroin through the disruption of noncovalent interactions, Bioconjugate Chem. 31 (2020) 1307–1312, https://doi.org/10.1021/acs.bioconjchem.0c00168.

[83] J. Ju, N. Hu, D.M. Cairns, H. Liu, B.P. Timko, Photo–cross-linkable, insulating silk fibroin for bioelectronics with enhanced cell affinity, Proc. Natl. Acad. Sci. USA 117 (2020) 15482–15489, https://doi.org/10.1073/pnas.2003696117.

[84] D.N. Rockwood, et al., Materials fabrication from Bombyx mori silk fibroin, Nat. Protoc. 6 (2011) 1612.

[85] C.Z. Zhou, et al., Fine organization of Bombyx mori fibroin heavy chain gene, Nucleic Acids Res. 28 (2000) 2413–2419, https://doi.org/10.1093/nar/28.12.2413.

[86] O. Hasturk, et al., Cytoprotection of human progenitor and stem cells through encapsulation in alginate templated, dual crosslinked silk and silk–gelatin composite hydrogel microbeads, Advanced Healthcare Materials 11 (2022), 2200293, https://doi.org/10.1002/adhm.202200293.

[87] J.K. Sahoo, et al., Sugar functionalization of silks with pathway-controlled substitution and properties, Adv. Biol. 5 (2021), 2100388, https://doi.org/10.1002/adbi.202100388.

[88] Y. Yu, Y. Chau, One-step "click" method for generating vinyl sulfone groups on hydroxyl-containing water-soluble polymers, Biomacromolecules 13 (2012) 937–942, https://doi.org/10.1021/bm2014476.

[89] C.D. Davidson, et al., Myofibroblast activation in synthetic fibrous matrices composed of dextran vinyl sulfone, Acta Biomater. 105 (2020) 78–86, https://doi.org/10.1016/j.actbio.2020.01.009.

[90] J.K. Sahoo, et al., Silk degumming time controls horseradish peroxidase-catalyzed hydrogel properties, Biomater. Sci. 8 (2020) 4176–4185, https://doi.org/10.1039/D0BM00512F.

[91] M.W. Ellzy, J.O. Jensen, J.G. Kay, Vibrational frequencies and structural determinations of di-vinyl sulfone, Spectrochim. Acta Mol. Biomol. Spectrosc. 59 (2003) 867–881, https://doi.org/10.1016/S1386-1425(02)00239-1.

[92] X. Hu, D. Kaplan, P. Cebe, Determining beta-sheet crystallinity in fibrous proteins by thermal analysis and infrared spectroscopy, Macromolecules 39 (2006) 6161–6170, https://doi.org/10.1021/ma0610109.

[93] A. Sundarakrishnan, Y. Chen, L.D. Black, B.B. Aldridge, D.L. Kaplan, Engineered cell and tissue models of pulmonary fibrosis, Adv. Drug Deliv. Rev. 129 (2018) 78–94, https://doi.org/10.1016/j.addr.2017.12.013.

[94] S. Khunmanee, Y. Jeong, H. Park, Crosslinking method of hyaluronic-based hydrogel for biomedical applications, J. Tissue Eng. 8 (2017), 2041731417726464, https://doi.org/10.1177/2041731417726464.

[95] N.R. Raia, et al., Enzymatically crosslinked silk-hyaluronic acid hydrogels, Biomaterials 131 (2017) 58–67, https://doi.org/10.1016/j.biomaterials.2017.03.046.

[96] F. Agostinacchio, X. Mu, S. Dirè, A. Motta, D.L. Kaplan, In situ 3D printing: opportunities with silk inks, Trends Biotechnol. 39 (2021) 719–730, https://doi.org/10.1016/j.tibtech.2020.11.003.

[97] E. Ruoslahti, Rgd and other recognition sequences for integrins, Annu. Rev. Cell Dev. Biol. 12 (1996) 697–715, https://doi.org/10.1146/annurev.cellbio.12.1.697.

[98] L. Buscemi, et al., The single-molecule mechanics of the latent TGF-beta1 complex, Curr. Biol. 21 (2011) 2046–2054, https://doi.org/10.1016/j.cub.2011.11.037.

[99] G. Jenkins, The role of proteases in transforming growth factor-β activation, Int. J. Biochem. Cell Biol. 40 (2008) 1068–1078, https://doi.org/10.1016/j.biocel.2007.11.026.

[100] J.H.W. Distler, et al., Shared and distinct mechanisms of fibrosis, Nat. Rev. Rheumatol. 15 (2019) 705–730, https://doi.org/10.1038/s41584-019-0322-7.

[101] M. Lodyga, B. Hinz, TGF-β1 - a truly transforming growth factor in fibrosis and immunity, Semin. Cell Dev. Biol. 101 (2020) 123–139, https://doi.org/10.1016/j.semcdb.2019.12.010.

[102] T.A. Wynn, Cellular and molecular mechanisms of fibrosis, J. Pathol. 214 (2008) 199–210, https://doi.org/10.1002/path.2277PMID-18161745.

[103] K. Janssens, et al., Camurati-Engelmann disease: review of the clinical, radiological, and molecular data of 24 families and implications for diagnosis and treatment, J. Med. Genet. 43 (2006) 1–11, https://doi.org/10.1136/jmg.2005.033522.

[104] I. Arestrom, B. Zuber, T. Bengtsson, N. Ahlborg, Measurement of human latent transforming growth factor-β1 using a latency associated protein-reactive ELISA, J. Immunol. Methods 379 (2012) 23–29, https://doi.org/10.1016/j.jim.2012.02.016.

[105] M. Sacchi, R. Bansal, J. Rouwkema, Bioengineered 3D models to recapitulate tissue fibrosis, Trends Biotechnol. 38 (2020) 623–636, https://doi.org/10.1016/j.tibtech.2019.12.010.

[106] B.-M. Chen, T.-L. Cheng, S.R. Roffler, Polyethylene glycol immunogenicity: theoretical, clinical, and practical aspects of anti-polyethylene glycol antibodies, ACS Nano 15 (2021) 14022–14048, https://doi.org/10.1021/acsnano.1c05922.